Correlating active layer structure and composition with device performance and lifetime in amino acid modified perovskite solar cells

Chieh-Ting Lin[a,b], Weidong Xu[b], Thomas J. Macdonald[b], Jonathan Ngiam[a], Ju-Hyeon Kim[c], Tian Du[a,b], Shengda Xu[a], Pabitra Shakya Tuladhar[b], Hongkyu Kang[c], Kwanghee Lee[c], James R .Durrant*[b,d] and Martyn A. McLachlan*[a]

[a] Department of Materials and Centre for Processable Electronics, Molecular Sciences Research Hub, Imperial College London, London W12 0BZ , UK
[b] Department of Chemistry and Centre for Processable Electronics, Molecular Sciences Research Hub, Imperial College London, London W12 0BZ , UK
[c] Heeger Center for Advanced Materials and Research Institute for Solar and Sustainable Energies, Gwangju Institute of Science and Technology, Gwangju, 61005 Republic of Korea
[d] SPECIFIC IKC, College of Engineering, Swansea University, Bay Campus, Fabian Way, Swansea SA1 8EN, UK

*Corresponding authors: j.durrant@imperial.ac.uk; martyn.mclachlan@imperial.ac.uk

Keywords: perovskite solar cell; photoluminescence; $MAPbI_3$; amino acids; additive engineering; SIMS.

Abstract

Additive engineering is emerging as a powerful strategy to further enhance the performance of perovskite solar cells (PSCs), with the incorporation of bulky cations and amino acid (AA) derivatives being shown as a promising strategy for enhanced device stability. However, the incorporation of such additives typically results in photocurrent losses owing to their saturated carbon backbones hindering charge transport and collection. Here we investigate the use of amino acids with varying carbon chain lengths as zwitterionic additives that enhance PSC device stability, in air and nitrogen, under illumination. We discover that stability is insensitive to chain length however, as anticipated photocurrent drops as chain length increases. Using glycine as an additive results in an improvement in open circuit voltage from 1.10 to 1.14 V and a resulting power conversion efficiency of 20.2% (20.1% stabilized). Using time-of-flight secondary ion mass spectrometry we confirm that the AAs reside at the surfaces and interfaces of our perovskite films and propose the mechanisms by which stability is enhanced. We highlight this with glycine as an additive, whereby an 8-fold increase in device lifetime in ambient air at 1-sun illumination is recorded. Short circuit photoluminescence quenching of complete devices are reported and reveal that the loss in photocurrent density observed with longer carbon chain AAs results from inefficient charge extraction from the perovskite absorber layer. These combined results demonstrate new fundamental understandings in the photophysical processes of additive engineering using amino acids and provide a significant step forward in improving the stability of high-performance PSCs.

1. Introduction

Whilst significant efforts have been made to obtain power conversion efficiencies (PCEs) exceeding 25 % in perovskite solar cells (PSCs) in parallel there has been a tremendous research focus directed at addressing stability issues in PSCs .[1–3] Several layers in complete device stacks are susceptible to degradation by processes including electrode corrosion [4] and interfacial degradation[5] however it is the intrinsic instability of the perovskite absorber that must be addressed if long-term stability is to be achieved.[3] A number of extrinsic factors including moisture, heat, bias, oxygen and light have been identified as causes of perovskite degradation.[6] To overcome these issues numerous sophisticated strategies have been proposed, including additive engineering, incorporating superoxide scavengers and metal–organic frameworks (MOFs), introducing hydrophobic interlayers and halide substitutional doping.[7–11] Of these strategies, additive engineering is seen as an effective means of improving stability and often, in parallel, improving device PCE.[12–15] For example, the addition of quaternary ammonium halides is reported as an efficient means of improving shelf-stability in ambient air [13] whilst crosslinking species *i.e.* butylphosphonic acid 4-ammonium chloride and p-amino-benzoic acid can greatly improve moisture sensitivity. [14,15] Of the factors influencing degradation, the combination of oxygen and light are identified as significant factors limiting the lifetime of unencapsulated devices operating in air[6,9,16,17] as their combination results in degradation driven by superoxide (O_2^-) formation.[18] Notably, in screen printed methyl ammonium lead iodide ($MAPbI_3$) devices the incorporation of low concentrations of aminovaleric acid (AVA) as a processing additive results in improved operational stability in air.[8,19] Whilst stability enhancements can be achieved in most studies where AVA is used as an additive a reduced short circuit current density (J_{sc}) is normally observed.[7,19,20] Similar reductions in J_{sc} have been reported with other bulky cation addivites,[21,22] however the origin of these J_{sc} reductions are typically overlooked and their origins remain unexplored.

Photoluminescence (PL) measurements are regarded as an effective means of evaluating recombination and charge transfer in perovskite films, perovskite/charge transport layer (CTL) junctions, and complete devices. PL in perovskite films is related to the electronic trap states,[23] and the PL quenching efficiency (PLQE) of the transport layer can be used to evaluate the charge transfer of the perovskite/CTL junction. It has recently been reported that the PL quenching of the entire device is voltage-dependent, indicating the PL of the complete device (device PL) under different voltages can reflect the J-V characteristics of the device. These observations show that PL measurements can effectively evaluate the recombination and charge transfer in solar cells and be used to probe the origins of J_{sc} variations.

The large variety of defects that may exist at/near the perovskite surface can give rise to electronic trap states with a wide range of energies, however, the charged nature of many of these defects means that passivation can be achieved by a variety of ionic bonding and coordinate bonding strategies.[24] The carboxylic and amine end groups of AVA are considered advantageous owing to their zwitterionic nature as the positive and negative terminations of the molecule can bond to, thus passivate, surface cationic and anionic defects. Indeed reports employing perovskite quantum dots suggest that their zwitterionic nature gives rise to a dual passivation effect.[25] In the case of AVA, we have previously demonstrated that the additive preferentially locates on the surfaces and interfaces of perovskite grains. However, the aliphatic chain between end groups may act as a barrier to charge

extraction in devices.[8] Integrating a conjugated core to such molecules has been explored as one strategy to defect passivation,[26] and here we investigate modifying the aliphatic chain length, whilst preserving the end group functionality using four AAs with various carbon chain length, namely AVA (4C), γ-aminobutyric acid (3C), β-alanine (2C) and glycine (1C), **Figure 1a**. These materials have been investigated as interface modifiers [27,28] and additives in mesoporous PSCs[19] where they are reported to improve device performance by promoting the formation of low-dimensional perovskite phases at surfaces and grain boundaries.[26,29] However, their incorporation aa additives in planar PSCs remain unexplored. We investigate the incorporation of these AAs into $MAPbI_3$ PSCs and demonstrate a universal improvement in stability against oxygen induced photodegradation. Surprisingly the stability enhancement is insensitive to changes in AA chain length, however in parallel an observed reduction in J_{sc} occurs as chain length increases. We find that the J_{sc} reductions correlate with steady-state photoluminescence quenching (PLQ) measurements, providing direct evidence of reduced charge transfer as chain length increases. Strikingly, the addition of glycine (1C) results in an increase in open circuit voltage (V_{oc}) from 1.10 V to 1.14 V without associated J_{sc} losses, resulting in champion devices with a stabilized PCE of 20.1 %. Devices with glycine as an additive also exhibit the greatest unencapsulated operational stability. This work successfully investigates and explains reductions in J_{sc} observed with additive incorporation and outlines an effective strategy employing the AA glycine as a PCE and stability enhancing additive. Overall our results reveal a range of morphological modifications that occur when incorporating the AAs. Specifically, a reduction in grain size as aliphatic chain length increases. Hence, the choice of glycine as the optimum additive is made by balancing the structural modifications with the zwitterionic nature of the end groups ability to passivate surface defects, the reduced PL quenching and taking into consideration the aliphatic chain and its role in impeding charge collection. In many ways we can draw an analogy with perovskite quantum dot systems – not in length scale but acknowledging that in such systems the long aliphatic tails of passivating ligands can impede charge transfer and facilitate the radiative recombination in the perovskite.

2. Results and discussion

2.1 Film deposition and device preparation

PSCs were prepared with a structure (layer thickness in parentheses) of glass/ITO/PTAA(10 nm)/PFN (<10 nm)/ $MAPbI_3$ (300 nm)/PCBM(50nm)/BCP (<10nm)/Cu (100 nm), full details are given in experimental methods. A typical device cross-sectional scanning electron microscopy (SEM) image is shown in **Figure S1**. Here the $MAPbI_3$ solutions were prepared by dissolving 1.5 mol dm^{-3} methyl ammonium iodide (MAI) and 1.5 mol dm^{-3} PbI_2 in a solvent mixture of DMF/DMSO (8.9:1.1 volume ratio). Solutions of the AAs were prepared by dissolving AAs in deionized water each to a concentration of 1.5 mol dm^{-3}. The perovskite thin films were prepared by spin-coating 1.5 mol dm^{-3} of the MAI/PbI_2 solutions with and without the addition of 1-2 vol. % of the various AAs, reference cells were also prepared using only deionized water. All films were aged in dry air under LED arrays with 1 sun illumination intensity for 1-3 hours. For device preparation PCBM and BCP were sequentially solution processed prior to thermal evaporation of Cu as a top contact. Where extended lifetime testing was carried out Cu was replaced by Cr (3.5nm)/Au(100nm) the eliminate concerns around electrode stability/oxidation.

2.2 Performance of planar structure perovskite solar cell employing amino acid additives

We first consider the device performance of PSCs with the AAs added at a concentration of 1 vol. %, the J-V characteristics of which are shown in **Figure 1b**. The devices prepared with glycine (1C) are comparable to, if not subtly better than additive free devices - however the measured PCE values for devices prepared with the longer carbon chain additives decrease with increasing chain length, driven by significant reductions in J_{sc}. The average device parameters are shown in **Table S1**. This behavior is consistent with recent work by Huang and co-workers where bilateral alkylamine molecules with various carbon chain lengths were employed.[30] The values of hysteresis index for the water treated and 1C devices are close to zero, and lower than the pristine devices whilst HI increases with increased aliphatic chain length. [31] The external quantum efficiency (EQE) measurements, **Figure S2**, agree well with the measured device J_{sc} values. Increasing the concentration of the AAs to 2 vol %, **Figure 1c,** unsurprisingly results in significant J_{sc} losses in devices prepared with 2C-4C chain length AAs, **Figure 1d**, however devices prepared using glycine again show improved performance characteristics compared to the additive free device. Noticeably, the PCE of devices containing 2 vol. % glycine improved from 18.99 (± 0.49), to 19.54 (± 0.21%) reaching 19.86 (±0.31%) in additive free, 1 vol. % and 2 vol. % films respectively. In the later the performance increase is driven by an increase in V_{oc} from 1.10 (±0.01V) to 1.14 (±0.01V) compared to the reference devices whilst Jsc was maintained. The champion cell, prepared with 2 vol. % glycine (1C), achieved a PCE of 20.2 % in both forward and reverse scan directions (0.1 V s^{-1}) and a stabilized PCE of 20.1%. (**Figure 1e**).

2.3 Thin film stability

Figure 2a highlights the 12 – 15 °2θ range of the X-ray diffraction (XRD) patters for films aged for 1 and 3 hours with the various AAs at 1 vol. %, an additive free reference film is also included to allow fair comparison of the data. The same data are plotted separately using a semi-log scale in **Figure S3**. This XRD region is very sensitive to structural changes, as it contains the major diffraction peak of $MAPbI_3$ (110) around 14.1°2θ and also the major diffraction peak of the degradation product PbI_2 (001) at 12.60° 2θ.[17,23,32] Considering the AA-free reference film a distinct PbI_2 peak is observed after 1 hour with the $MAPbI_3$ (110) disappearing, indicating near-complete degradation, after 3 hours ageing. In contrast, films prepared with AAs show no appreciable signs of PbI_2 formation after 1 hour aging, and after 3 hours show significantly less PbI_2 then in the additive free films.

Whilst such data should not be used to make a quantitative comparison between films, when comparing the intensity of the $MAPbI_3$ (110) to that of PbI_2 (001) in the AA films it appears that the amount of PbI_2 formed after 3 hours reduces as the chain length of the additive reduces. This can be ascribed to the reduced grain size/increased grain boundary concentration in the films prepared with longer chain length AAs (**Figure S4**), as oxygen induced photodegradation has been shown to initiate at grain boundaries.[33] The images in **Figure 2c** show photographs of the films before and after 3 hours ageing. The distinct yellow color seen in the aged additive free film is evidence of near complete degradation of $MAPbI_3$ to PbI_2 whereas the films with the AAs show no discernible color change. Thus, all of the AAs appear to be having an active role in preventing photodegradation, with some dependence on carbon chain length that originates from microstructural changes in the films.

2.4 Radiative recombination in perovskite solar cells with amino acid additives

Others have shown, that by introducing low concentrations of bulky cations into perovskite precursor solutions or subsequently depositing these materials on the surface of pre-formed perovskite films, significant PCE enhancements can be achieved.[21,22,34–36] Such improvements are driven by increases in V_{oc}, explained by a variety of defect passivation mechanisms, however in parallel reductions in device J_{sc} are often observed. [21,2237] In recent work we have shown that charge transfer from the perovskite to the charge transporting layers (CTLs) can be inhibited when bulky cation concentrations exceed specific low concentrations, [37] but in contrast note that in the perovskite light emitting diode (PeLED) literature significantly higher concentrations of such additives can be tolerated.[38,39] We propose here that the J_{sc} losses in PSCs originate from a reduction in charge transfer *i.e.* increased bimolecular (radiative) recombination losses in the perovskite whilst operated at short-circuit.

To validate this hypothesis, photoluminescence quenching (PLQ) measurements were conducted on bare perovskite films on glass and on completed devices at short circuit. Whilst thin film PLQ measures have been extensively reported in the literature there are remarkably few reports of PLQ in complete devices.[40,41] Here, for the first time, we employ a combination of thin film and complete device PLQ measurements to evaluate short-circuit current losses in devices. Schematic illustrations of the processes occurring under these different conditions are shown in **Figure 3,** where PL_{SC}/PL_{PVK} represents the proportion of charge carriers that radiatively recombine in the device at short circuit relative to a perovskite film thin film *i.e.* in the absence of CTLs.

2.5 Photoluminescence quenching of $MAPI_3$ films

All PL measurements were carried out under 1 Sun equivalent illumination. In the first instance we studied the steady state (PL_{PVK}) of perovskite thin films on glass, **Figure 4a**. A significant increase in PL intensity (approx. 6-fold) is observed in all 1 vol. % AA films compared with the AA-free reference films. This is accompanied by longer PL lifetimes (Figure S4) that are generally related to reduced charge trapping. These observations confirm that the non-radiative trap density has been reduced, which can be explained by the carboxyl group or amine groups bonding with the Pb-I framework, passivating surface defects. [42,43] We also observed blue shifts of the PL peak in AA films compared with the reference films, such blue shifts have been shown to correlate with the removal of surface defects in perovskite films.[44] **Figure 4b** shows the PL spectra of perovskite films sandwiched between the electron (PCBM) and hole (PTAA) CTLs (PL_{CTLs}). It is well established that under illumination films interfaced with CTLs will transfer a large proportion of free charge carries to the CTLs, thus strong PL quenching will occur,[45] and indeed significant quenching is observed in all films here. The data in **Figures 4a-b** is summarized into the plot shown in **Figure 4c.** To investigate further differences in the PL behavior of films with and without CTLs, the calculated PL_{CTLs}/PL_{PVK} values are plotted in **Figure 4d**. Interestingly the additive free and film with glycine added obtain comparable PL_{CTLs}/PL_{PVK} values, around 10 %, whilst in contrast films with longer carbon chain length AAs have PL_{CTLs}/PL_{PVK} values of around 30 %. This indicates that the AA-free films and those prepared with glycine show similar behavior in terms of the transfer of photogenerated charge carriers to the respective CTLs, whereas the efficiency of this charge transfer is significantly impeded where 2-4 carbon chain length AAs are added, resulting in greater radiative recombination in the bulk.

2.6 Photoluminescence quenching of devices at open and short circuit

Device PL measurements have been demonstrated to be an effective and unambiguous *in-operando* approach to assessing the charge carrier extraction efficiency in perovskite PV devices.[41,46,47] Recently we have shown that dramatic PL quenching occurs when an efficient device is switched from open to short circuit, owing to the efficient charge collection at short-circuit. [46] Given that device PL at open circuit is analogous to PL_{CTLs}, we can now combine CTL PL quenching with device PL quenching.

An illustration of the PL emission measurement of complete devices at open and short circuit conditions is shown in **Figure 5a**. The corresponding PL spectra for AA-free and the devices prepared with the AAs are shown **Figure 5b-f**, where the device PL intensities are normalized by the device PL_{OC}. There is a clear increase in the PL_{SC} as the AA carbon chain length increases. The calculated PL_{SC}/PL_{OC} is plotted in **Figure 5g** and shows that PL_{SC}/PL_{OC} gradually increased from 10% to 60% when the carbon chain length increases, indicating that the charge carrier extraction induced by switching from open to short circuit becomes less efficient as the chain length is increased. Again, we find that the device incorporating glycine as an additive shows comparable PL_{SC}/PL_{OC} behavior to the reference cell suggesting equally efficient charge extraction in the additive based device. By combining the values of PL_{CTLs}/PL_{PVK} from thin film PL in **Figure 4d** and PL_{SC}/PL_{OC} from device PL in **Figure 5g** we can calculate the PL accumulation moving from a film to a device at short circuit. The ratio of PL_{SC}/PL_{PVK} is calculated as:

$$PL_{SC}/PL_{PVK} = (PL_{CTLs}/PL_{PVK}) * (PL_{SC}/PL_{OC}) \qquad \textit{equation 1}$$

where PL_{SC}/PL_{PVK} represents the density of charge carriers remaining in the perovskite film within the device at short circuit relative to an uncontacted perovskite film, and so is quantification of the overall extraction efficiency at short circuit under one sun irradiation. **Figure 5h** plots the PL_{SC}/PL_{PVK} and J_{sc} of the corresponding devices. As expected, the trend of PL_{SC}/PL_{PVK} is inverse to that of device Jsc, where current density drops with increasing carbon chain length of the AA. This observation provides direct evidence that the loss of J_{sc} with increased carbon chain length results from increased bimolecular recombination in devices operated at short-circuit conditions. The increasing aliphatic chain length of the AAs clearly hinders charge extraction. However, the 1C AA, glycine, shows comparable PL_{SC}/PL_{PVK} and Jsc as the reference cell, with an enhanced V_{oc} resulting from defect passivation – and thus an enhancement in PCE.

2.8. Mass Spectra Analysis

To identify and locate the AAs we employed time-of-flight secondary ion mass spectrometry (ToF-SIMS). The data show that the AAs reside on the surfaces and grain boundaries of the perovskite films. We chose aminovaleric acid (4C) and glycine (1C) as the extremes of carbon chain length. In order to achieve statistically sound data - given the large number of variables that could influence the mass spectra three ITO/poly(triaryl amine)(PTAA)/$MAPbI_3$/AA samples for each AA were fabricated. In each sample, mass spectra were obtained from four different areas giving a total of twelve mass spectra for each precursor solution. Measurements were performed with low applied ion dose densities of less than 1.0×10^{12} ions/cm^2. For all obtained mass spectra, achieving static conditions in which mass spectra obtained are representative of the true

surface rather than pre-bombarded areas. **Figure 6** shows the mass spectra obtained from AA-free reference films in addition to films with AVA and glycine. Considering the glycine films firstly, a mass peak assigned to $[Gly\text{-}H]^-$ (m/z = 74.024) can be distinguished that is absent in the other films (Figure 6a). Similarly, Figures 6b-c, show two distinct mass features in the AVA films that can be assigned to $[AVA\text{-}H]^-$ (m/z = 116.07) and $[AVA]^-$ (m/z = 117.08). The mass fragments identified are characteristic of each of the AAs used and no similar peaks are observed in the AA-free reference films. Therefore, we can conclude that the addition of glycine and AVA to precursor solutions has an effect on their overall surface composition of the $MAPbI_3$ films.

2.7 Device stability and iodide diffusion

We have thus far focused on the origins of device efficiency changes in PSCs prepared with AAs, we now turn to consider the role these additives play in stability against photodegradation. As electrode instability can contribute to device degradation during extended testing, here a Cr/Au bilayer is used to minimize such effects.[48] **Figure 7a** shows the normalized PCE vs. time of AA-free and 1 vol. % glycine devices tested in N_2 under 1 Sun illumination. The AA-free device drops 15 % of the initial PCE (t_{85} lifetime) after 192 hours whereas the device with the added glycine takes some 420 hours to reach t_{85}. Degradation in air is faster for the same devices, Figure 7b, with the AA-free reference reaching t_{85} after only 10 hours testing compared with 80 hours for the 1 vol % glycine device. In order to probe any potential morphological changes that may be occurring during lifetime testing we again employed XRD to characterize the structure of our $MAPbI_3$ films before and after testing, both with and without glycine added, **Figure 7c**. It's important to note that here we anticipate slower degradation owing to the presence of the ETL and the electrode that can function as a superoxide scavenger and oxygen barrier respectively. [9] This is evidenced by the relatively small quantities of PbI_2 observed in the AA-free reference cell even after 120 hours testing however in the same reference device we see evidence of a structural rearrangement occurring prior to the onset of significant degradation. Specifically, a shoulder appears on the low 2θ side of the $MAPbI_3$ (110) diffraction peak. It is not uncommon to see asymmetry in the $MAPbI_3$ (110) diffraction peak owing to the underlying (002) peak of the tetragonal phase being stabilized at room temperature.[49] Hence the apparent absence of the PbI_2 (001) peak normally associated with degradation does not eliminate structural transitions associated with extended lifetime testing, [4] that does not occur in the presence of glycine. The same data are plotted separately using a semi-log scale in Figure S6. From our ToF-SIMs analysis and previous work with AVA we know that such additives preferentially locate at surfaces and grain boundaries, [8] hence may be providing a steric barrier to reorganization or there may be an energetic barrier to their mobility that infers stability. Whilst we cannot be conclusive as to the origins of this behavior the evidence for a morphological change is compelling.

Finally, in order to further provide insights into the vertical distribution of ions as a function of operational time, dynamic ToF-SIMS was employed to analyze how the AAs influence chemical depth profiles, particularly the susceptibility of ion diffusion. For all aged devices I^- (m/z = 126.92) is observed on the electrode surfaces and both I^- (m/z = 126.92) and I_2^-(m/z= 253.8) at the electrode/BCP interface (**Figure 7d**). In the AA-free device, the concentration of I^- is much higher within the electrode/BCP/PCBM layers. This suppressed diffusion of I^- observed with AA incorporation is symptomatic of a more stable absorber layer, supported by the reduced

decomposition of devices incorporating glycine under oxygen and light stress (Figure 2a) and enhanced device stability in Figure 7a. Analyzing $Pb_xI_y^-$profiles (**Figure 7e**), there are no significant differences that can be observed. Considering the ratios of Pb-based mass fragments, there does not seem to be any chemical changes within the absorber layer between the samples. Thus, given that significant differences in only I^- (m/z = 126.92) were observed, diffusion of I^- is likely to be accountable for the reduction in measured device stabilities.

3. Discussion

We have demonstrated a strategy to enhance the intrinsic stability of $MAPbI_3$ against oxygen induced photodegradation by incorporating AAs with various aliphatic chain lengths as processing additives. Interestingly, all of the additives investigated yield comparable stability enhancements yet dramatic differences in PCE are observed. The change in PCE correlates with changes in the AA carbon chain length, where increases in chain length leads to J_{sc} reductions and overall reductions in PCE. Utilizing a suite of steady state PL quenching techniques, including standalone thin films and films interfaces with charge transport layers (PVK-to-CTLs) and carrying out open to short circuit quenching (OC-to-SC) on complete devices we provide direct experimental evidence that the J_{sc} losses observed with longer carbon chain additives correlate with a reduction in charge extraction efficiency.

Incorporating AAs into $MAPbI_3$ has several advantages. Firstly, incorporating glycine (1C) results in enhancements of device V_{oc}, from 1.10 to 1.14V in planar PSCs. This is attributed to defect passivation, which is supported by the enhanced PL yield seen (**Figure 4a**). Defect passivation is a well-known strategy for reducing non-radiative recombination losses and improving V_{oc}.[24,50] Interestingly the AAs investigated all improve stability against oxygen induced photodegradation. AAs are amongst the best known zwitterions that should, in principle, allow for the passivation of anionic and cationic defects by a single molecule. In the case where one defect is predominant the AAs remain able to passivate – unlike other common additives that may be *either* anionic or cationic. In the case of oxygen induced photodegradation, which has been shown to be induced by superoxide attack on halide vacancies,[18,51] then the carboxyl group of the AAs will be involved in defect passivation. This behavior also helps explain the enhancements in operational stability observed in both N_2 and dry air, with the former a lifetime more than double (t_{85}) that of additive free devices is seen, 420 hours compared with 192 hours. In inert conditions ion migration, facilitated by surface defects, has been shown to contribute to accelerated degradation[52] – this can however be minimized by additives that preferentially locate at grain boundaries.[53–55]

Using ToF-SIMS we show that the AAs locate preferentially on film surfaces and interfaces *i.e.* grain boundaries which provides compelling evidence that surface passivation lies at the origin of the enhanced stability against oxygen induced degradation. It should be noted that spatial variations cannot be captured in these measurements as the beam conditions have not been optimised for sch. Even when optimised, the highest spatial resolution obtainable would be on the order of microns. The discussed scattering data and mass spectra thus only provide evidence of the AA presence on the surface of the samples but are unable to spatially resolve their location. We can therefore consider possible bonding mechanisms for hydrogen and ionic bonding between functional groups and the film surfaces that would explain the observed increased photostability and

enhancement in device properties. [8,37] In the case of the functional groups present in the AAs carboxyl groups (R –COOH) can undergo hydrogen bonding with under-coordinated I atoms on the surface whilst the amine groups(R $–NH_2$), that will be protonated in solution (R $–NH_3^+$) can undergo hydrogen bonding with surface dangling bonds. [56]Furthermore, ionic bonding can occur between $–COO^–$ and $V_i^{\bullet}$ and/or under-coordinated Pb.

The rather short lifetimes (t_{85}) observed in air are anticipated owing to the additional degradation pathways available in addition to contributions from oxidation of interlayers and contacts. Nonetheless the impact of AA addition was beneficial, with devices incorporating glycine exhibiting an 8-fold lifetime increase compared with additive free devices. We note that this is, to-date, one of the best reported lifetimes for planar structured PSCs that have undergone maximum power-point ageing without encapsulation.[57]

Interestingly, the AAs also have a strong influence in the grain size observed in our polycrystalline films, **Figure S1**. There is a direct relationship between increases in grain size and improvements in J_{sc}, thus PCE, which is anticipated [58,59] however the ability to stabilize smaller grains may be attractive to the PeLED community as bimolecular recombination is more likely. [58–62] Thus our results also allow us to begin to correlate microstructural modulations with photophysical measurements with the grain size changes here likely contribute to the significant charge transfer and PL_{SC}/PL_{PVK} changes in the $MAPbI_3$ with different AAs.

4. Conclusions

In summary, we have demonstrated the incorporation of a range of AAs into $MAPbI_3$ based perovskite solar cells that result in reductions in oxygen induced photodegradation. Enhanced stability is observed with all of the AAs investigated, however there is a noticeable reduction in J_{sc} and consequently PCE as the carbon chain length of the AAs increase. We provide direct evidence that these J_{sc} losses correlate with the increased PL_{SC}/PL_{PVK} ratio of devices held at short circuit and also directly probe the location of the AAs, confirming their presence on grain surfaces and interfaces. Comparing the microstructure of the $MAPbI_3$ with the various AAs there is also an observed modification in grain size, whereby an inverse relationship exists with the chain length of the AA *i.e.* longer aliphatic chains result in smaller grains, which negatively impacts charge transfer efficiency. Thus, we conclude that the AAs investigated universally offer a means of stabilizing devices against oxygen induced photodegradation however the aliphatic nature of the molecule means that charge extraction is hindered when larger AAs are incorporated. Using glycine, with only one carbon between the amino and carboxyl groups of the molecule, improvements in device power conversion efficiency can be achieved whilst simultaneously extending the lifetime. The incorporation of AAs into the perovskite active layer therefore provides a simple strategy for improving performance and lifetime of unencapsulated perovskite solar cells.

Experimental Methods

Device fabrication and characterization:

The ITO substrates were cleaned by sequentially washing in an ultrasonic bath with detergent, deionized water, acetone and isopropanol before being dried under a stream on N_2 and treated with UV-ozone immediately prior to use. Poly(triaryl)amine (PTAA) solution (2mg/ml in chlorobenzene) was spin-coated on the ITO at 3000 rpm

for 20 seconds. PFN (0.5mg/ml in methanol) was spin-coated on the substrate at 5000 rpm for 20 seconds to modify the wettability. The perovskite solution was spin-coated on substrates at 4000 rpm for 30 seconds. At 7 seconds, 0.4ml diethyl ether was dripped on the substrate. The substrates were annealed at 60 °C for 2 minutes and then at 100 °C for 60 minutes. During the annealing process, the substrate was covered by a petri dish. After the thermal annealing process, the phenyl-C61-butyric acid methyl ester (PCBM) solution (40mg/ml in chlorobenzene) was passed through a 0.45 μm filter spin-coated on the substrate. The bathocuproine (BCP) solution (0.5mg/ml in methanol) was spin-coated on the substrate. Finally, 100nm Cu was evaporated as top electrode. For the device aged under dry air and illumination, Cr (3.5nm)/Au(100nm) was used to prevent electrode oxidation. J-V characteristics were measured under Air Mass 1.5G global (AM 1.5G) illumination. J-V scans were obtained at a scan rate of 100mV $s^{-1,}$ controlled by a Keithley 236 sourcemeter.

A Bentham PVE300 photovoltaic QE system was used to obtain the EQE spectrum over the wavelength range 300 -800nm. Device stability was measured in dry air or in N_2 with 1 sun illumination provided by an array of LEDs with devices held at their maximum power point (mpp) during the measurement. The light intensity of LEDs was calibrated by reaching the same J_{sc} of PSCs measured under AM 1.5G filtered xenon lamp.

Scanning electron microscopy (SEM) and X-ray diffraction

A Leo Gemini 1525 Field Emission Scanning Electron Microscope (FE-SEM) was used to obtain SEM images. All samples were coated with a 5nm Cr layer. The working distance was between 2-5mm and the working voltage was fixed at 5 kV. XRD data were obtained using a Bruker D2 Phaser instrument operating at 40 kV and 40 mA with aged devices measured using a PANalytical X'Pert Pro Multi-Purpose Diffractometer (MPD) at the same operational conditions.

Thin film photoluminescence and device photoluminescence

All perovskite thin films and devices were sealed before measurements. PL was obtained using a Horiba Jobin Yvon Fluorolog system with the light source provided by 550nm CW laser with the intensity equivalent to 1 sun.

Time-of-Flight Mass Spectrometry (ToF-SIMS)

ToF-SIMS was performed using the TOF.SIMS5 (IONTOF) instrument. For static measurements, a 25 kV Bi_3^+ primary ion beam was used to raster an analysis area of 150 μm x 150 μm with 128 pixels x 128 pixels in the 'interlaced' mode. The dose was kept at < 1 x 10^{12} ions/cm^2 to ensure static conditions. For depth-profile measurements, an O_2^+ sputter beam at 1 kV and 220nA was rastered over an area of 300 μm x 300 μm within which the primary ion beam (as above) was rastered. The primary-ion analysis mode was high-current bunched mode (HCBM) for higher mass resolution.

Acknowledgements

We gratefully acknowledge the Global Research Laboratory (GRL) Program through the National Research Foundation of Korea (NRF) funded by the Ministry of Science and ICT (NRF-2017K1A1A2013153) and the EPSRC

Plastic Electronics CDT (EP/L016702/1) and GCRF Sunrise project (EP/P032591/1) for financial support. W.X would like to thank the financial support from China Scholarship Council. T.D gratefully acknowledges the Stephan and Anna Hui scholarship for supporting his doctoral studies. T.J.M would like to thank the Royal Commission for the 1851 exhibition or their financial support through an 1851 Research Fellowship.

Supporting Information

Cross-section SEM image of device structure; EQE spectra of $MAPbI_3$ devices with 1 vol. % amino acid additive; surface SEM images and grain size analysis; TCSPC spectra; Statistical J-V characteristics

References

(1) Jiang, Q.; Zhao, Y.; Zhang, X.; Yang, X.; Chen, Y.; Chu, Z.; Ye, Q.; Li, X.; Yin, Z.; You, J. Surface Passivation of Perovskite Film for Efficient Solar Cells. *Nat. Photonics* **2019**, *13* (7), 460–466.

(2) Meng, L.; You, J.; Yang, Y. Addressing the Stability Issue of Perovskite Solar Cells for Commercial Applications. *Nat. Commun.* **2018**, *9* (1), 5265.

(3) Wang, R.; Mujahid, M.; Duan, Y.; Wang, Z. K.; Xue, J.; Yang, Y. A Review of Perovskites Solar Cell Stability. *Adv. Funct. Mater.* **2019**, *29*, 1808843.

(4) Lin, C.-T.; Ngiam, J.; Xu, S.; Chang, Y.-H.; Du, T.; Macdonald, T. J.; Durrant, J.; McLachlan, M. Enhancing the Operational Stability of Unencapsulated Perovskite Solar Cells through Cu-Ag Bilayer Electrode Incorporation. *J. Mater. Chem. A* **2020**, *8*, 8684–8691.

(5) Kim, J.; Lee, Y.; Yun, A. J.; Gil, B.; Park, B. Interfacial Modification and Defect Passivation by the Cross-Linking Interlayer for Efficient and Stable CuSCN-Based Perovskite Solar Cells. *ACS Appl. Mater. Interfaces* **2019**, *11* (50), 46818–46824.

(6) Bryant, D.; Aristidou, N.; Pont, S.; Sanchez-Molina, I.; Chotchunangatchaval, T.; Wheeler, S.; Durrant, J. R.; Haque, S. A. Light and Oxygen Induced Degradation Limits the Operational Stability of Methylammonium Lead Triiodide Perovskite Solar Cells. *Energy Environ. Sci.* **2016**, *9* (5), 1655–1660.

(7) Grancini, G.; Roldán-Carmona, C.; Zimmermann, I.; Mosconi, E.; Lee, X.; Martineau, D.; Narbey, S.; Oswald, F.; De Angelis, F.; Graetzel, M.; Nazeeruddin, M. K. One-Year Stable Perovskite Solar Cells by 2D/3D Interface Engineering. *Nat. Commun.* **2017**, *8*, 15684.

(8) Lin, C. T.; De Rossi, F.; Kim, J.; Baker, J.; Ngiam, J.; Xu, B.; Pont, S.; Aristidou, N.; Haque, S. A.; Watson, T.; McLachlan, M. A.; Durrant, J. R. Evidence for Surface Defect Passivation as the Origin of the Remarkable Photostability of Unencapsulated Perovskite Solar Cells Employing Aminovaleric Acid as a Processing Additive. *J. Mater. Chem. A* **2019**, *7* (7), 3006–3011.

(9) Lin, C.-T.; Pont, S.; Kim, J.; Du, T.; Xu, S.; Li, X.; Bryant, D.; McLachlan, M. A.; Durrant, J. R. Passivation against Oxygen and Light Induced Degradation by the PCBM Electron Transport Layer in Planar Perovskite Solar Cells. *Sustain. Energy Fuels* **2018**, *2*, 1686–1692.

(10) Bai, Y.; Dong, Q.; Shao, Y.; Deng, Y.; Wang, Q.; Shen, L.; Wang, D.; Wei, W.; Huang, J. Enhancing Stability and Efficiency of Perovskite Solar Cells with Crosslinkable Silane-Functionalized and Doped Fullerene. *Nat. Commun.* **2016**, *7*, 1–9.

(11) Lee, C. C.; Chen, C. I.; Liao, Y. Te; Wu, K. C. W.; Chueh, C. C. Enhancing Efficiency and Stability of Photovoltaic Cells by Using Perovskite/Zr-MOF Heterojunction Including Bilayer and Hybrid Structures. *Adv. Sci.* **2019**, *6* (5), 1801715.

(12) Zuo, L.; Guo, H.; DeQuilettes, D. W.; Jariwala, S.; De Marco, N.; Dong, S.; DeBlock, R.; Ginger, D. S.; Dunn, B.; Wang, M.; Yang, Y. Polymer-Modified Halide Perovskite Films for Efficient and Stable Planar Heterojunction Solar Cells. *Sci. Adv.* **2017**, *3* (8), 1–12.

(13) Zheng, X.; Chen, B.; Dai, J.; Fang, Y.; Bai, Y.; Lin, Y.; Wei, H.; Zeng, X. C.; Huang, J. Defect Passivation in Hybrid Perovskite Solar Cells Using Quaternary Ammonium Halide Anions and Cations. *Nat. Energy* **2017**, *2* (7), 17102.

(14) Yun, S. C.; Ma, S.; Kwon, H. C.; Kim, K.; Jang, G.; Yang, H.; Moon, J. Amino Acid Salt-Driven Planar Hybrid

Perovskite Solar Cells with Enhanced Humidity Stability. *Nano Energy* **2019**, *59* (December 2018), 481–491.

(15) Li, X.; Ibrahim Dar, M.; Yi, C.; Luo, J.; Tschumi, M.; Zakeeruddin, S. M.; Nazeeruddin, M. K.; Han, H.; Grätzel, M. Improved Performance and Stability of Perovskite Solar Cells by Crystal Crosslinking with Alkylphosphonic Acid ω -Ammonium Chlorides. *Nat. Chem.* **2015**, *7* (9), 703–711.

(16) Leijtens, T.; Bush, K.; Cheacharoen, R.; Beal, R.; Bowring, A.; McGehee, M. D. Towards Enabling Stable Lead Halide Perovskite Solar Cells; Interplay between Structural, Environmental, and Thermal Stability. *J. Mater. Chem. A* **2017**, *5* (23), 11483–11500.

(17) Pont, S.; Bryant, D.; Lin, C.-T.; Aristidou, N.; Wheeler, S.; Ma, X.; Godin, R.; Haque, S. A.; Durrant, J. R. Tuning $CH_3NH_3Pb(I_{1-x}Br_x)_3$ Perovskite Oxygen Stability in Thin Films and Solar Cells. *J. Mater. Chem. A* **2017**, *5* (20), 9553–9560.

(18) Aristidou, N.; Eames, C.; Sanchez-Molina, I.; Bu, X.; Kosco, J.; Saiful Islam, M.; Haque, S. A. Fast Oxygen Diffusion and Iodide Defects Mediate Oxygen-Induced Degradation of Perovskite Solar Cells. *Nat. Commun.* **2017**, *8* (May), 15218.

(19) Mei, A.; Li, X.; Liu, L.; Ku, Z.; Liu, T.; Rong, Y.; Xu, M.; Hu, M.; Chen, J.; Yang, Y.; Grätzel, M.; Han, H. A Hole-Conductor–Free, Fully Printable Mesoscopic Perovskite Solar Cell with High Stability. *Science (80-.).* **2014**, *345* (6194), 295–298.

(20) Hu, Y.; Si, S.; Mei, A.; Rong, Y.; Liu, H.; Li, X.; Han, H. Stable Large-Area (10×10 Cm^2) Printable Mesoscopic Perovskite Module Exceeding 10% Efficiency. *Sol. RRL* **2017**, *1* (2), 1600019.

(21) Bai, Y.; Xiao, S.; Hu, C.; Zhang, T.; Meng, X.; Lin, H.; Yang, Y.; Yang, S. Dimensional Engineering of a Graded 3D–2D Halide Perovskite Interface Enables Ultrahigh V Oc Enhanced Stability in the p-i-n Photovoltaics. *Adv. Energy Mater.* **2017**, *7* (20), 1701038.

(22) Ye, T.; Bruno, A.; Han, G.; Koh, T. M.; Li, J.; Jamaludin, N. F.; Soci, C.; Mhaisalkar, S. G.; Leong, W. L. Efficient and Ambient-Air-Stable Solar Cell with Highly Oriented 2D@3D Perovskites. *Adv. Funct. Mater.* **2018**, *28* (30), 1–8.

(23) Du, T.; Kim, J.; Ngiam, J.; Xu, S.; Barnes, P. R. F.; Durrant, J. R.; McLachlan, M. A. Elucidating the Origins of Subgap Tail States and Open-Circuit Voltage in Methylammonium Lead Triiodide Perovskite Solar Cells. *Adv. Funct. Mater.* **2018**, *2* (1), 1801808.

(24) Chen, B.; Rudd, P. N.; Yang, S.; Yuan, Y.; Huang, J. Imperfections and Their Passivation in Halide Perovskite Solar Cells. *Chemical Society Reviews*. 2019, pp 3842–3867.

(25) Jia, D.; Chen, J.; Yu, M.; Liu, J.; Johansson, E. M. J.; Hagfeldt, A.; Zhang, X. Dual Passivation of CsPbI3 Perovskite Nanocrystals with Amino Acid Ligands for Efficient Quantum Dot Solar Cells. *Small* **2020**, *16* (24), 1–12.

(26) Hu, Y.; Zhang, Z.; Mei, A.; Jiang, Y.; Hou, X.; Wang, Q.; Du, K.; Rong, Y.; Zhou, Y.; Xu, G.; Han, H. Improved Performance of Printable Perovskite Solar Cells with Bifunctional Conjugated Organic Molecule. *Adv. Mater.* **2018**, *30* (11), 1705786.

(27) Shih, Y. C.; Lan, Y. B.; Li, C. S.; Hsieh, H. C.; Wang, L.; Wu, C. I.; Lin, K. F. Amino-Acid-Induced Preferential Orientation of Perovskite Crystals for Enhancing Interfacial Charge Transfer and Photovoltaic Performance. *Small* **2017**, *13* (22), 1–10.

(28) Shih, Y. C.; Wang, L. Y.; Hsieh, H. C.; Lin, K. F. Enhancing the Photocurrent of Perovskite Solar Cells via Modification of the TiO2/CH3NH3PbI3 Heterojunction Interface with Amino Acid. *J. Mater. Chem. A* **2015**, *3* (17), 9133–9136.

(29) Zheng, H.; Wu, W.; Xu, H.; Zheng, F.; Liu, G.; Pan, X.; Chen, Q. Self-Additive Low-Dimensional Ruddlesden–Popper Perovskite by the Incorporation of Glycine Hydrochloride for High-Performance and Stable Solar Cells. *Adv. Funct. Mater.* **2020**, *30* (15), 2000034.

(30) Wu, W. Q.; Yang, Z.; Rudd, P. N.; Shao, Y.; Dai, X.; Wei, H.; Zhao, J.; Fang, Y.; Wang, Q.; Liu, Y.; Deng, Y.; Xiao, X.; Feng, Y.; Huang, J. Bilateral Alkylamine for Suppressing Charge Recombination and Improving Stability in Blade-Coated Perovskite Solar Cells. *Sci. Adv.* **2019**, *5* (3), 1–10.

(31) Habisreutinger, S. N.; Noel, N. K.; Snaith, H. J. Hysteresis Index: A Figure without Merit for Quantifying Hysteresis in Perovskite Solar Cells. *ACS Energy Lett.* **2018**, *3* (10), 2472–2476.

(32) Du, T.; Burgess, C. H.; Kim, J.; Zhang, J.; Durrant, J. R.; McLachlan, M. A. Formation, Location and Beneficial Role of PbI 2 in Lead Halide Perovskite Solar Cells. *Sustain. Energy Fuels* **2017**, *1* (1), 119–126.

(33) Sun, Q.; Fassl, P.; Becker-Koch, D.; Bausch, A.; Rivkin, B.; Bai, S.; Hopkinson, P. E.; Snaith, H. J.; Vaynzof, Y. Role of Microstructure in Oxygen Induced Photodegradation of Methylammonium Lead Triiodide Perovskite Films. *Adv. Energy Mater.* **2017**, *7* (20), 1700977.

(34) Li, N.; Zhu, Z.; Chueh, C.-C.; Liu, H.; Peng, B.; Petrone, A.; Li, X.; Wang, L.; Jen, A. K.-Y. Mixed Cation FA $_{x}$ PEA $_{1-x}$ PbI $_{3}$ with Enhanced Phase and Ambient Stability toward High-Performance Perovskite Solar Cells. *Adv. Energy Mater.* **2017**, *7* (1), 1601307.

(35) Wang, F.; Geng, W.; Zhou, Y.; Fang, H.-H.; Tong, C.-J.; Loi, M. A.; Liu, L.-M.; Zhao, N. Phenylalkylamine Passivation of Organolead Halide Perovskites Enabling High-Efficiency and Air-Stable Photovoltaic Cells. *Adv. Mater.* **2016**, *28* (45), 9986–9992.

(36) Wang, Z.; Lin, Q.; Chmiel, F. P.; Sakai, N.; Herz, L. M.; Snaith, H. J. Efficient Ambient-Air-Stable Solar Cells with 2D-3D Heterostructured Butylammonium-Caesium-Formamidinium Lead Halide Perovskites. *Nat. Energy* **2017**, *2* (9), 17135.

(37) Lin, C.; Lee, J.; Kim, J.; Macdonald, T. J.; Ngiam, J.; Xu, B.; Daboczi, M.; Xu, W.; Pont, S.; Park, B.; Kang, H.; Kim, J.; Payne, D. J.; Lee, K.; Durrant, J. R.; McLachlan, M. A. Origin of Open-Circuit Voltage Enhancements in Planar Perovskite Solar Cells Induced by Addition of Bulky Organic Cations. *Adv. Funct. Mater.* **2020**, *30* (7), 1906763.

(38) Liu, X. K.; Gao, F. Organic-Inorganic Hybrid Ruddlesden-Popper Perovskites: An Emerging Paradigm for High-Performance Light-Emitting Diodes. *J. Phys. Chem. Lett.* **2018**, *9* (9), 2251–2258.

(39) Chen, Y.; Yu, S.; Sun, Y.; Liang, Z. Phase Engineering in Quasi-2D Ruddlesden-Popper Perovskites. *J. Phys. Chem. Lett.* **2018**, *9* (10), 2627–2631.

(40) Du, T.; Xu, W.; Xu, S.; Ratnasingham, S. R.; Lin, C.-T.; Kim, J.; Briscoe, J.; McLachlan, M.; Durrant, J. Light-Intensity and Thickness Dependent Efficiency of Planar Perovskite Solar Cells: Charge Recombination versus Extraction. *J. Mater. Chem. C* **2020**, *8* (36), 12648–12655.

(41) Stolterfoht, M.; Le Corre, V. M.; Feuerstein, M.; Caprioglio, P.; Koster, L. J. A.; Neher, D. Voltage-Dependent Photoluminescence and How It Correlates with the Fill Factor and Open-Circuit Voltage in Perovskite Solar Cells. *ACS Energy Lett.* **2019**, 2887–2892.

(42) Peng, J.; Khan, J. I.; Liu, W.; Ugur, E.; Duong, T.; Wu, Y.; Shen, H.; Wang, K.; Dang, H.; Aydin, E.; Yang, X.; Wan, Y.; Weber, K. J.; Catchpole, K. R.; Laquai, F.; De Wolf, S.; White, T. P. A Universal Double-Side Passivation for High Open-Circuit Voltage in Perovskite Solar Cells: Role of Carbonyl Groups in Poly(Methyl Methacrylate). *Adv. Energy Mater.* **2018**, *8* (30), 1801208.

(43) Luo, B.; Naghadeh, S. B.; Allen, A.; Li, X.; Zhang, J. Z. Peptide-Passivated Lead Halide Perovskite Nanocrystals Based on Synergistic Effect between Amino and Carboxylic Functional Groups. *Adv. Funct. Mater.* **2017**, *27* (6), 1604018.

(44) Shao, Y.; Xiao, Z.; Bi, C.; Yuan, Y.; Huang, J. Origin and Elimination of Photocurrent Hysteresis by Fullerene Passivation in CH3NH3PbI3 Planar Heterojunction Solar Cells. *Nat. Commun.* **2014**, *5*.

(45) Kim, J.; Godin, R.; Dimitrov, S. D.; Du, T.; Bryant, D.; McLachlan, M. A.; Durrant, J. R. Excitation Density Dependent Photoluminescence Quenching and Charge Transfer Efficiencies in Hybrid Perovskite/Organic Semiconductor Bilayers. *Adv. Energy Mater.* **2018**, 1802474.

(46) Du, T.; Xu, W.; Daboczi, M.; Kim, J.; Xu, S.; Lin, C.-T.; Kang, H.; Lee, K.; Heeney, M. J.; Kim, J.-S.; Durrant, J. R.; McLachlan, M. A. P-Doping of Organic Hole Transport Layers in p–i–n Perovskite Solar Cells: Correlating Open-Circuit Voltage and Photoluminescence Quenching. *J. Mater. Chem. A* **2019**, *7* (32), 18971–18979.

(47) Dreessen, C.; Pérez-del-Rey, D.; Boix, P. P.; Bolink, H. J. Radiative and Non-Radiative Losses by Voltage-Dependent in-Situ Photoluminescence in Perovskite Solar Cell Current-Voltage Curves. *J. Lumin.* **2020**, *222*, 117106.

(48) Domanski, K.; Correa-Baena, J. P.; Mine, N.; Nazeeruddin, M. K.; Abate, A.; Saliba, M.; Tress, W.; Hagfeldt, A.; Grätzel, M. Not All That Glitters Is Gold: Metal-Migration-Induced Degradation in Perovskite Solar Cells. *ACS Nano* **2016**, *10* (6), 6306–6314.

(49) Kavadiya, S.; Strzalka, J.; Niedzwiedzki, D. M.; Biswas, P. Crystal Reorientation in Methylammonium Lead Iodide Perovskite Thin Film with Thermal Annealing. *J. Mater. Chem. A* **2019**, *7* (20), 12790–12799.

(50) Qiu, L.; He, S.; Ono, L. K.; Qi, Y. Progress of Surface Science Studies on ABX3-Based Metal Halide Perovskite Solar Cells. *Advanced Energy Materials*. 2020, p 1902726.

(51) Aristidou, N.; Sanchez-Molina, I.; Chotchuangchutchaval, T.; Brown, M.; Martinez, L.; Rath, T.; Haque, S. A. The Role of Oxygen in the Degradation of Methylammonium Lead Trihalide Perovskite Photoactive Layers. *Angew. Chemie Int. Ed.* **2015**, *54* (28), 8208 –8212.

(52) Domanski, K.; Roose, B.; Matsui, T.; Saliba, M.; Turren-Cruz, S. H.; Correa-Baena, J. P.; Carmona, C. R.; Richardson, G.; Foster, J. M.; De Angelis, F.; Ball, J. M.; Petrozza, A.; Mine, N.; Nazeeruddin, M. K.; Tress, W.; Grätzel, M.; Steiner, U.; Hagfeldt, A.; Abate, A. Migration of Cations Induces Reversible Performance Losses over Day/Night Cycling in Perovskite Solar Cells. *Energy Environ. Sci.* **2017**, *10* (2), 604–613.

(53) Lee, J. W.; Dai, Z.; Han, T. H.; Choi, C.; Chang, S. Y.; Lee, S. J.; De Marco, N.; Zhao, H.; Sun, P.; Huang, Y.; Yang, Y. 2D Perovskite Stabilized Phase-Pure Formamidinium Perovskite Solar Cells. *Nat. Commun.* **2018**, *9* (1), 3201.

(54) Shao, Y.; Fang, Y.; Li, T.; Wang, Q.; Dong, Q.; Deng, Y.; Yuan, Y.; Wei, H.; Wang, M.; Gruverman, A.; Shield, J.; Huang, J. Grain Boundary Dominated Ion Migration in Polycrystalline Organic–Inorganic Halide Perovskite Films. *Energy Environ. Sci.* **2016**, *501*, 395–398.

(55) Bai, S.; Da, P.; Li, C.; Wang, Z.; Yuan, Z.; Fu, F.; Kawecki, M.; Liu, X.; Sakai, N.; Wang, J. T.-W.; Huettner, S.; Buecheler, S.; Fahlman, M.; Gao, F.; Snaith, H. J. Planar Perovskite Solar Cells with Long-Term Stability Using Ionic Liquid Additives. *Nature* **2019**, *571* (7764), 245–250.

(56) Aydin, E.; De Bastiani, M.; De Wolf, S. Defect and Contact Passivation for Perovskite Solar Cells. *Adv. Mater.* **2019**, *31*, 1900428.

(57) Yu, D.; Hu, Y.; Shi, J.; Tang, H.; Zhang, W.; Meng, Q.; Han, H.; Ning, Z.; Tian, H. Stability Improvement under High Efficiency—next Stage Development of Perovskite Solar Cells. *Sci. China Chem.* **2019**, *62* (6), 684–707.

(58) Du, T.; Burgess, C. H.; Lin, C.-T.; Eisner, F.; Kim, J.; Xu, S.; Kang, H.; Durrant, J. R.; McLachlan, M. A. Probing and Controlling Intragrain Crystallinity for Improved Low Temperature–Processed Perovskite Solar Cells. *Adv. Funct. Mater.* **2018**, *28* (51), 1803943.

(59) Nie, W.; Tsai, H.; Asadpour, R.; Neukirch, A. J.; Gupta, G.; Crochet, J. J.; Chhowalla, M.; Tretiak, S.; Alam, M. A.; Wang, H. High-Efficiency Solution-Processed Perovskite Solar Cells with Millimeter-Scale Grains. *Science (80-.).* **2015**, *347* (6221), 522–525.

(60) Ban, M.; Zou, Y.; Rivett, J. P. H.; Yang, Y.; Thomas, T. H.; Tan, Y.; Song, T.; Gao, X.; Credington, D.; Deschler, F.; Sirringhaus, H.; Sun, B. Solution-Processed Perovskite Light Emitting Diodes with Efficiency Exceeding 15% through Additive-Controlled Nanostructure Tailoring. *Nat. Commun.* **2018**, *9*, 3892.

(61) Song, J.; Li, J.; Xu, L.; Li, J.; Zhang, F.; Han, B.; Shan, Q.; Zeng, H. Room-Temperature Triple-Ligand Surface Engineering Synergistically Boosts Ink Stability, Recombination Dynamics, and Charge Injection toward EQE-11.6% Perovskite QLEDs. *Adv. Mater.* **2018**, *30*, 1800764.

(62) Wang, H.; Zhang, X.; Wu, Q.; Cao, F.; Yang, D.; Shang, Y.; Ning, Z.; Zhang, W.; Zheng, W.; Yan, Y.; Kershaw, S. V.; Zhang, L.; Rogach, A. L.; Yang, X. Trifluoroacetate Induced Small-Grained CsPbBr 3 Perovskite Films Result in Efficient and Stable Light-Emitting Devices. *Nat. Commun.* **2019**, *10*, 665.

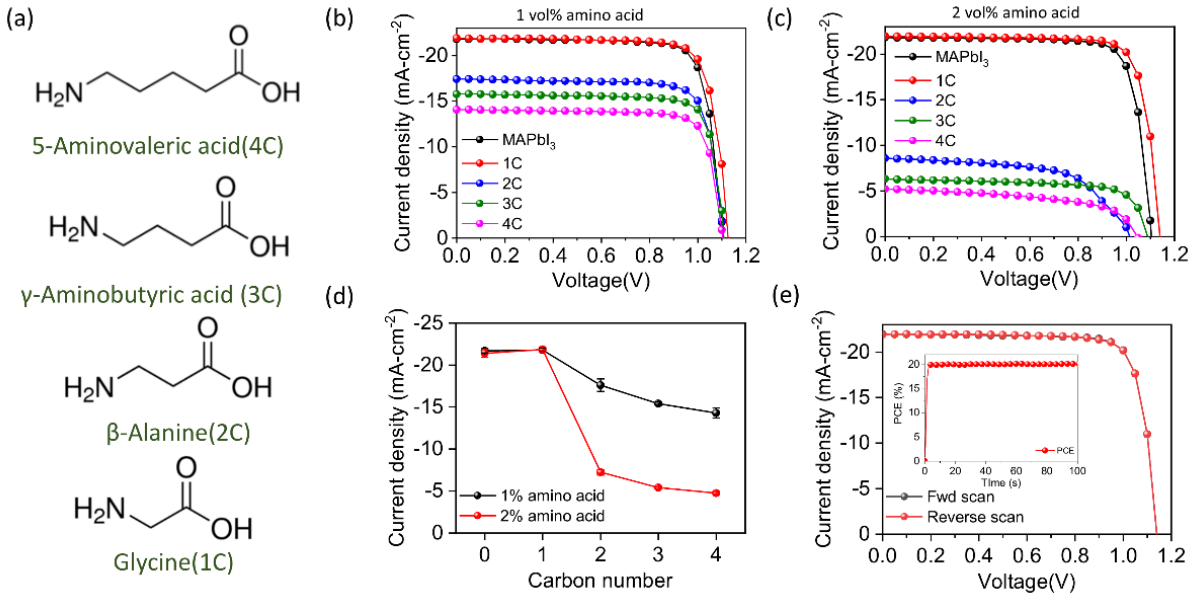

Figure 1 (a) Amino acids (AAs) employed as additives. J-V characterization of perovskite solar cells with (b) 1 vol. %, and (c) 2 vol. % of the AAs added to the active layer during processing. (d) Average short-circuit current density (J_{sc}) of devices with 1 vol. % and 2 vol. % of the amino acid additives. (e) Forward and reverse J-V scan of the champion device. Inset figure shows the stabilized PCE tracked at the maximum power point. Note: the $MAPbI_3$ reference cells in (b-c) and the 0 Carbon number data in (d) were prepared using 1-2 vol. % deionized water free from any AAs.

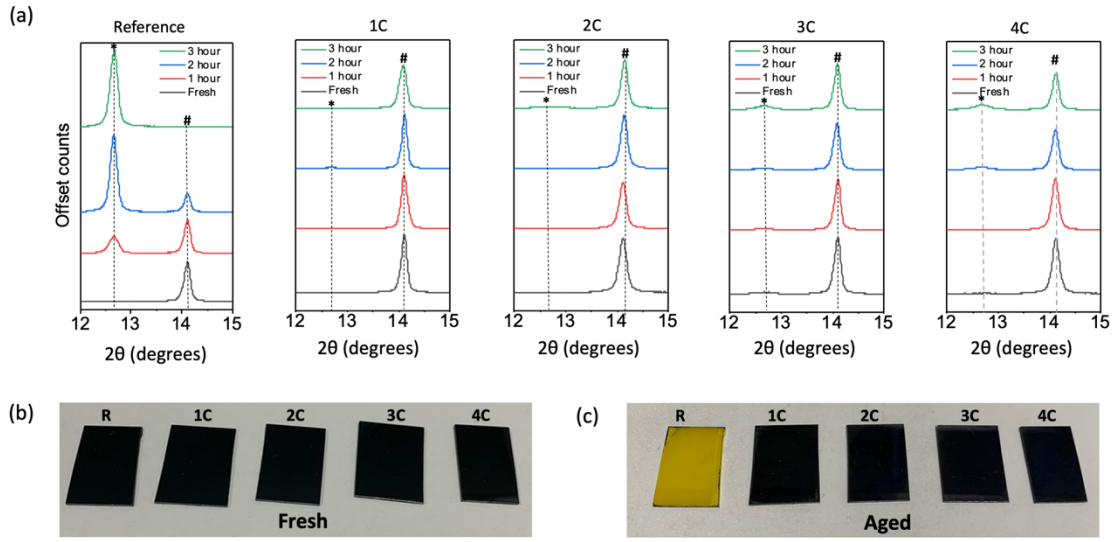

Figure 2 (a) XRD patterns, highlighting the $MAPbI_3$ $^{\#}$ (110) and PbI_2 * (001) diffraction peaks, for $MAPbI_3$ reference and $MAPbI_3$/amino acid films as-prepared (fresh) and after ageing. (b-c) photographs showing fresh and aged films, the yellow color seen in the aged reference (R) film is attributed to near complete degradation of $MAPI_3$ to PbI_2.

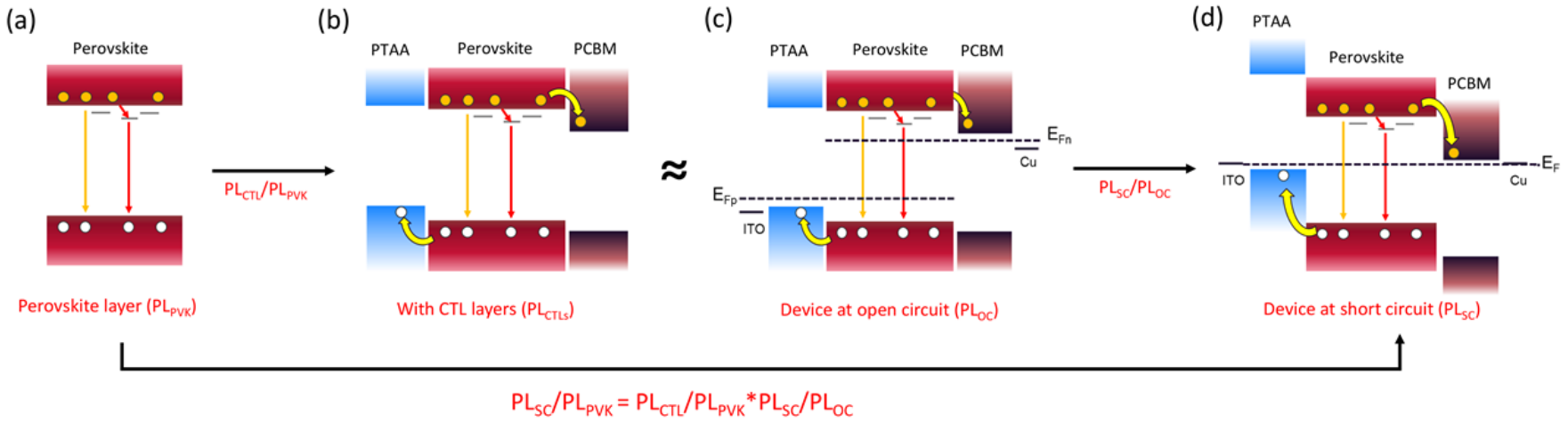

Figure 3 Schematic diagram of PL quenching measurements indicating which parameters are extracted from which specific conditions. (a) bare $MAPbI_3$ (b) $MAPbI_3$ interfaced with charge selective interlayers (CTLs) (c) complete device held at open circuit, and (d) complete device held at short circuit.

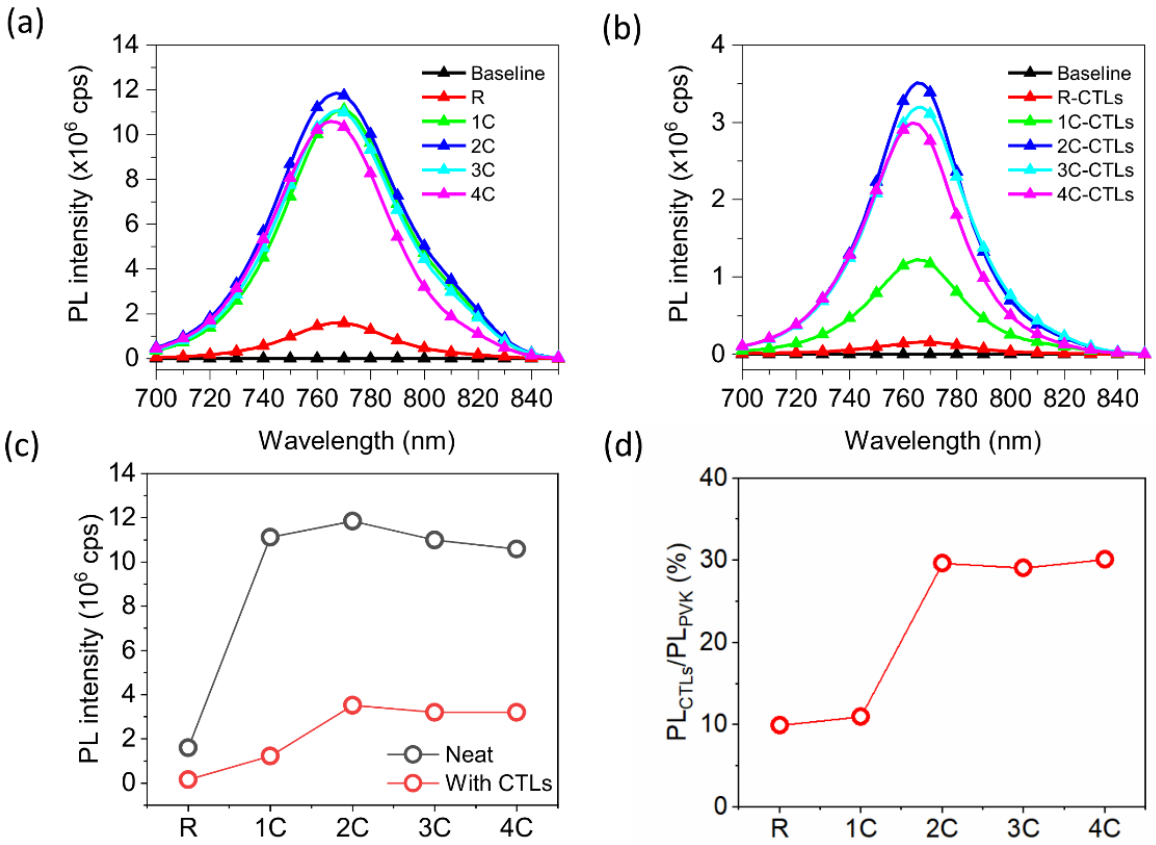

Figure 4 Steady state PL emission spectra of additive free and 1 vol. % amino acid as additive for (a) glass/$MAPbI_3$ and (b) glass/PTAA/PFN/$MAPBI_3$/PCBM. (c) absolute PL peak intensity from a-b replotted to allow comparison, and (d)PL_{CTLs}/PL_{PVK} derived from Figure 4a-b.

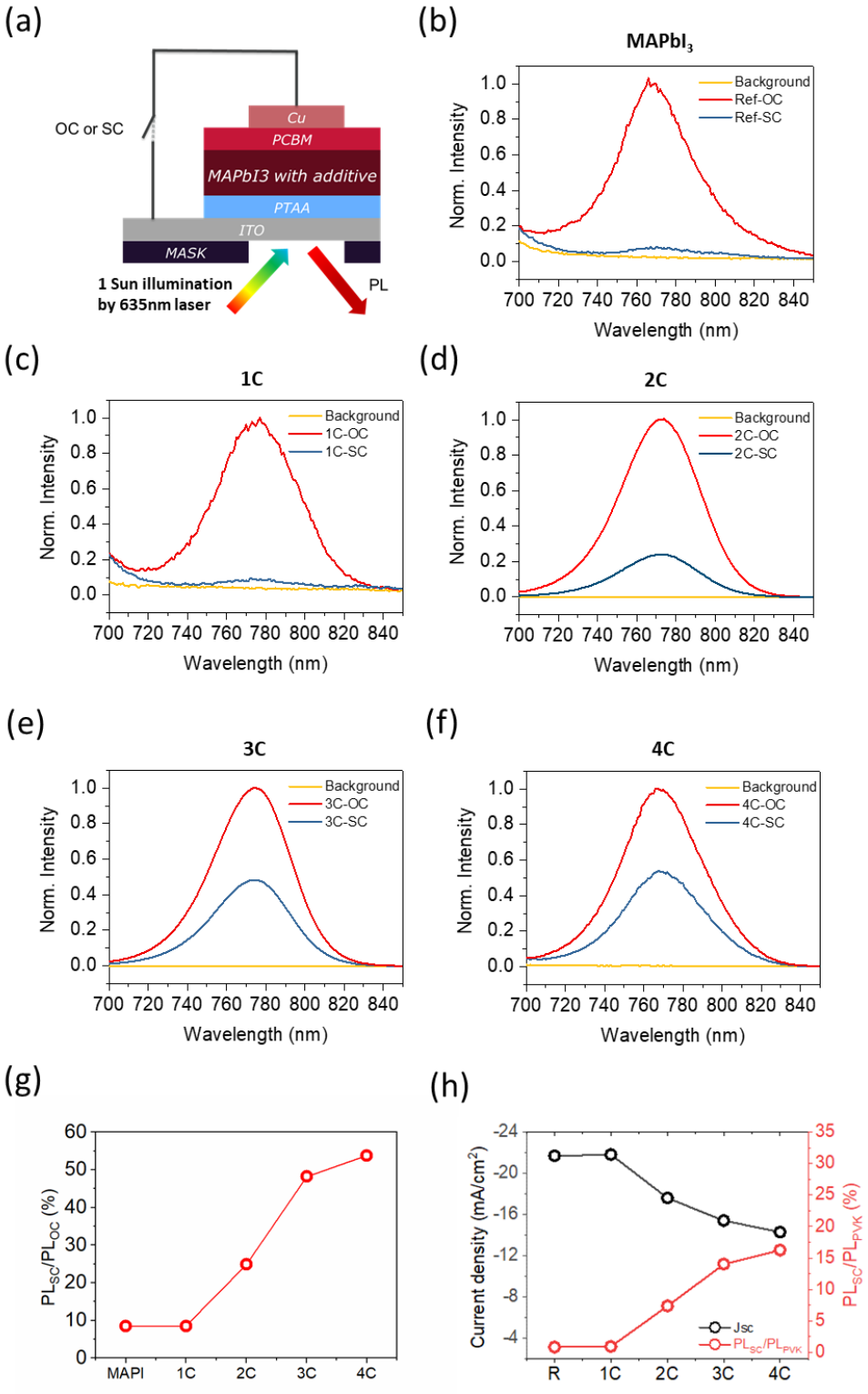

Figure 5 (a) Schematic diagram of device PL emission measurement. PL emission spectra of complete devices employing (b) neat $MAPbI_3$ and $MAPbI_3$ with 1 vol. % (c) glycine (d) β-alanine (e) γ-aminobutyric acid (f) 5-aminovaleric acid at both open and short circuit conditions. (g) calculated PL_{SC}/PL_{OC}. (h) The current density of PSCs employing amino acid additives and the PL_{SC}/PL_{PVK} of the corresponding devices.

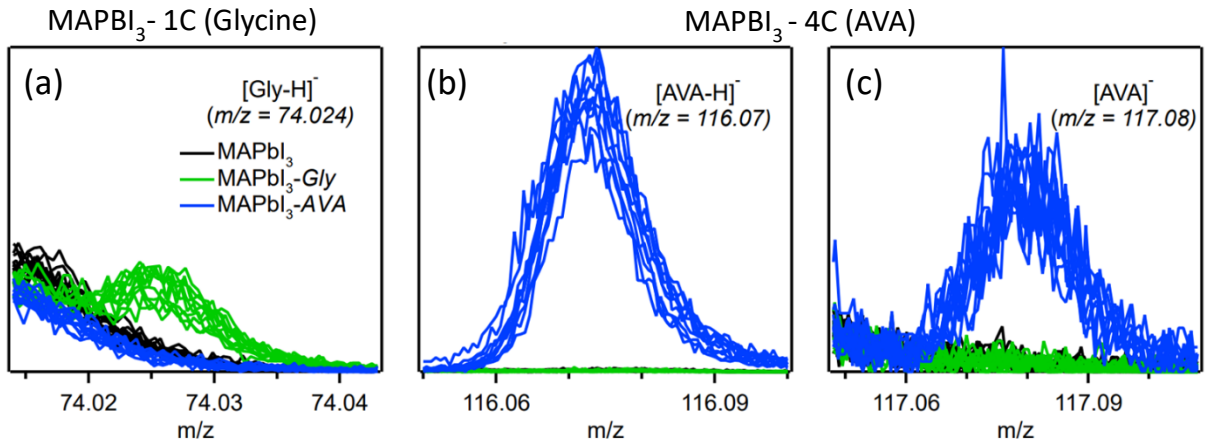

Figure 6. Selected m/z peaks of static ToF-SIMS (negative polarity) identified from fragmentation of or ionization of amino acid additives.(a) $[Gly\text{-}H]^-$ m/z = 74.024, (b) $[AVA\text{-}H]^-$ m/z = 116.07 and (c) $[AVA]^-$ (m/z = 117.08). The mass fragments identified are characteristic of the individual AAs used.

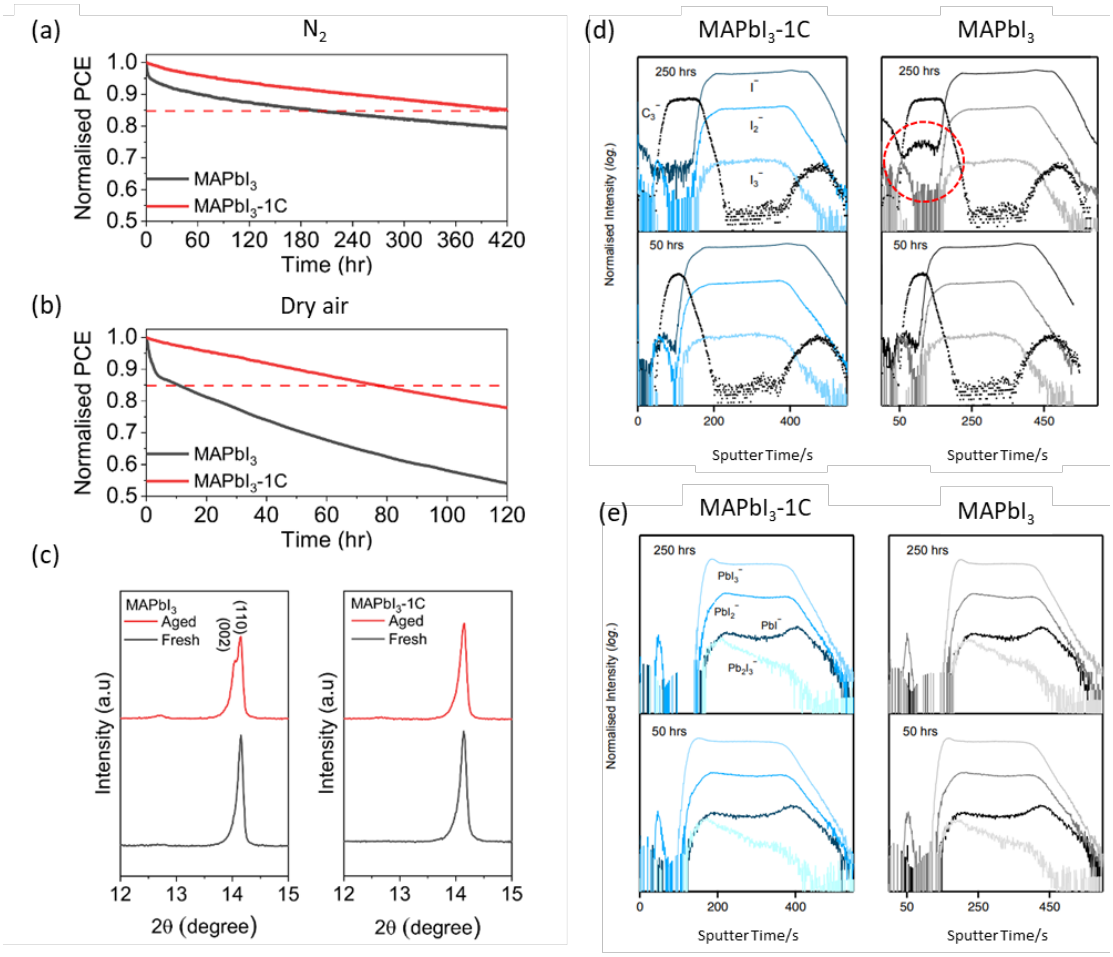

Figure 7 Device stability (maximum power point) of $MAPbI_3$ with and without glycine under 1 sun illumination in (a) N_2 and (b) dry air, the dashed vertical line indicates a drop in 15 % of the initial PCE (t_{85} lifetime) (c) XRD patterns focusing on the $MAPbI_3^{\#}$ (110) and PbI_2^{*} (001) diffraction regions of devices aged under full sun illumination in dry air for 120 hours. Note the onset of peak splitting observed in the $MAPbI_3^{\#}$ (110) on ageing. ToF-SIMS depth-profiles of $MAPbI_3$ and $MAPbI_3$-1C (with glycine) devices after 50 and 250 hours of oxygen and light stress showing (d) I_x^- species with a significant accumulation of I_3^- at the HTL/$MAPbI_3$ interface , highlighted by red dashed circle, after 250 hours as opposed to the relatively suppressed signal in $MAPbI_3$-1C and (e) PbI_x^- species with no observable difference between the two samples.

#